Eur. Phys. J. A **13**, 163–167 (2002)

**THE EUROPEAN PHYSICAL JOURNAL A**
© Società Italiana di Fisica
Springer-Verlag 2002

# Measurement of the interaction cross-section and related topics

A. Ozawa

RIKEN, 2-1 Hirosawa, Wako-shi, Saitama 351-0198, Japan

Received: 1 May 2001 / Revised version: 28 July 2001

**Abstract.** Recent experimental results concerning interaction cross-sections ($\sigma_{\rm I}$) are reviewed. The $\sigma_{\rm I}$ values were measured by a transmission method using the fragment separator at GSI. The $\sigma_{\rm I}$ values for B, C, N, O and F isotopes and the recently measured $\sigma_{\rm I}$ for Ar are presented. As related topics, an analysis by the recently developed Glauber model for a few-body system is introduced. By using this analysis, the effective density distributions for light neutron-rich nuclei can be deduced. The recently shown magic number $N = 16$ near to the neutron drip line is also discussed.

**PACS.** 21.10.Gv Mass and neutron distributions – 25.60.Dz Interaction and reaction cross sections

## 1 Introduction

After the pioneering work at LBL [1], the interaction cross-sections ($\sigma_{\rm I}$) have been extensively measured for light unstable nuclei ($A \leq 30$). Measurements of $\sigma_{\rm I}$ at relativistic energies (around 1 $A$ GeV) have allowed one to deduce the effective nuclear-matter radii using Glauber model calculations in the optical-limit approximation (GMOL) [1]. Since the isotope dependence of the nuclear radii is sensitive to the halo structure, measurements of $\sigma_{\rm I}$ have also been used to search for halo nuclei, for example, $^{11}$Li [1]. A unique opportunity to compare nuclear-matter and charge radii over a wide range of neutron numbers lies in Na isotopes. The root-mean-square (RMS) charge radii have been determined by isotopes shift measurements [2]. Because $\sigma_{\rm I}$ data can provide their matter radii, the RMS neutron radii for a chain of Na isotopes were deduced in the mass range from $A = 20$ to 32. A monotonic increase in the neutron skin thickness has been observed as the neutron number increases in Na isotopes [3].

On the experimental side, measurements of $\sigma_{\rm I}$ have a large feasibility. The measurements have no limitation of accessible species. One can measure $\sigma_{\rm I}$ even for a low-intensity beam, down to 0.01 cps; at that rate one can determine $\sigma_{\rm I}$ with 5% accuracy by measurements carried out over a period of a few days. Thus, recently, measurements of $\sigma_{\rm I}$ have reached to the proton and neutron drip lines up to O isotopes.

## 2 Experimental procedure and results

$\sigma_{\rm I}$ has been measured by a transmission-type experiment [1]. The cross-section was calculated by the equation

$$\sigma_{\rm I} = \frac{1}{N_{\rm t}} \log\left(\frac{\gamma_0}{\gamma}\right), \qquad (1)$$

where $\gamma$ is the ratio of the number of non-interacting nuclei to the number of incoming nuclei for a target in run, and $\gamma_0$ is the same ratio for an empty-target run. The number of target nuclei per cm$^2$ is written as $N_{\rm t}$. Particle identification is necessary upstream and downstream of the reaction target. As one of typical experimental setup for measurements, the experimental setup at FRS [4] is shown in fig. 1. Secondary beams were produced through projectile fragmentation of a primary beam accelerated to around 1 $A$ GeV by the heavy-ion synchrotorn SIS. The first half of the FRS, down to the intermediate focal plane (F2), was used to separate and identify the incident secondary beams. Reaction targets of carbon were placed at F2. The second half of the FRS was used as a spectrometer to transport the non-interacting secondary beams, which were identified and counted at the final focal plane of the FRS (F4). Particle identification was performed by $B\rho$-TOF-$\Delta E$ methods in this setup.

In order to secure the full transmission for non-interacting nuclei in the second half of the FRS, incident nuclei with a small angular divergence ($\leq \pm 9$ mrad) were selected based on the position information on the TPCs at F2. For $^{12}$C the present value of $\sigma_{\rm I}$ is consistent with the value obtained at LBL. The measured $\sigma_{\rm I}$ values are shown as a function of the neutron number ($N$) for boron, carbon, nitrogen, oxygen and fluorine isotopes in fig. 2. The observed $\sigma_{\rm I}$'s increase monotonically with $N$. It is noted that the rate of increase with $N$ changes at $N = 15$. The solid lines in fig. 2 show the $\sigma_{\rm I}$ values calculated using the equation

$$\sigma_{\rm I} = \pi(R_{\rm I}(^{12}{\rm C}) + r_0 A^{\frac{1}{3}})^2, \qquad (2)$$

where $R_{\rm I}(^{12}{\rm C})$ is the interaction radius of $^{12}$C (2.61 fm) and $r_0$ is selected to reproduce $\sigma_{\rm I}$ for $^{12}$C. In the neutron-rich side, the observed rate of increase is much larger than that calculated by eq. (2). This increase in the rate could

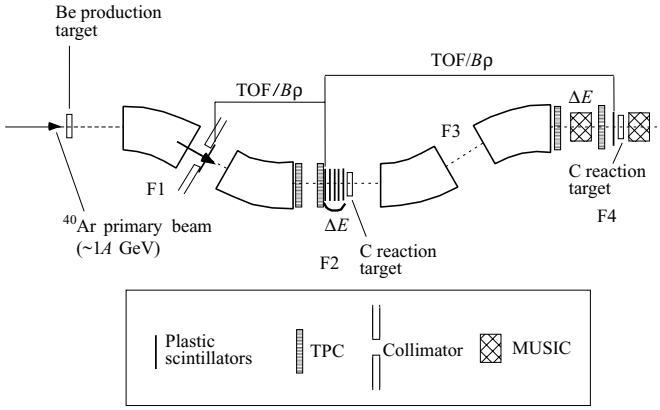


**Fig. 1.** Schematic view of the experimental setup at the fragment separator FRS.

indicate a thick neutron skin on the neutron-rich side. The observed $\sigma_{\rm I}$ for $^{19}$C is much larger than those of its neighbors, which supports a halo structure of this nucleus.

Very recently, the $\sigma_{\rm I}$ values for Ar isotopes ($A = 31$ to 40) have been measured at the FRS in GSI. Preliminary data show a strong neutron number dependence of $\sigma_{\rm I}$. Both on the proton- and neutron-rich sides, the measured $\sigma_{\rm I}$'s are larger than those calculated by eq. (2), which implies the existence of skins on the proton- and neutron-rich sides. The analysis is still in progress.

## 3 Related topics

### 3.1 Glauber model for a few-body system (GMFB)

GMOL has been widely used for deducing nuclear-matter radii from the interaction cross-sections and reaction cross-sections. However, Al-Khalili and Tostevin [5] have pointed out that it may not be a good approximation if one applies the model to loosely bound nuclei, such as neutron halo nuclei. This was also pointed out by Ogawa *et al.* in their calculation of $^{11}$Li [6]. In this refined model, a halo nucleus is decomposed into core and halo parts. In such a model, the wave function of a halo nucleus is written as

$$\Psi_0 = \varphi_0 \Phi_0, \tag{3}$$

where $\Phi_0$ is the core nucleus and the $\varphi_0$ is the halo neutron wave function in the ground state of a halo nucleus. In this case the reaction cross-section ($\sigma_{\rm reac}$) is written as

$$\sigma_{\rm reac} = \int {\rm d}b\{1 - \exp\left[-2{\rm Im}\chi_{\rm cT}(b)\right] \times |\langle\varphi_0| \sum_i \exp(i\chi_{{\rm n}_i{\rm T}}(b + s_i))|\varphi_0\rangle|^2\}, \tag{4}$$

where $i$ denote the neucleon in the halo and $\chi_{\rm cT}$ is a phase-shift function between the core nucleus and the target nucleus; $\chi_{\rm nT}$ is that between a neucleon and the target nucleus. Because the core nucleus is usually well bound, $\chi_{\rm cT}$ is calculated by the optical-limit approximation.

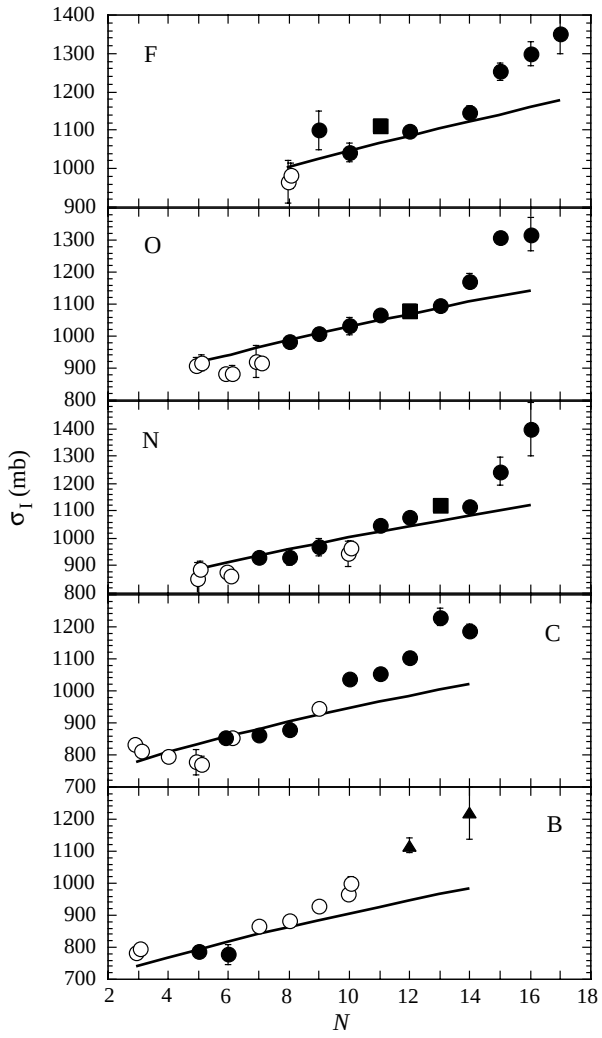


**Fig. 2.** Interaction cross-sections ($\sigma_{\rm I}$) for boron, carbon, nitrogen, oxygen and fluorine isotopes on carbon targets. The filled circles are data obtained at GSI. The open circles are data from previous studies at LBL.

Al-Khalili and Tostevin applied this method to $^{11}$Li, $^{11}$Be, and $^{8}$B halo nuclei for the first time [5], and found that this new model gives smaller cross-sections than those obtained from GMOL if one uses the same wave function. As a result, the deduced RMS matter radii of halo nuclei are 0.1 to 0.2 fm larger than that deduced from GMOL.

### 3.2 Effective density distributions for light neutron-rich nuclei

If we provide wave functions for the valence nucleon, we can estimate the effective densities using GMFB. A single-nucleon wave function can be calculated by a simple potential model. For example, the code WAVEFUNC [7] can solve the eigenvalue problem of the Schrödinger equation in the Woods-Saxon and Coulomb potentials. In this code, the single-nucleon wave function for the *s, p* and *d* orbitals in a $^{A-1}Z$ plus nucleon potential are obtained for various

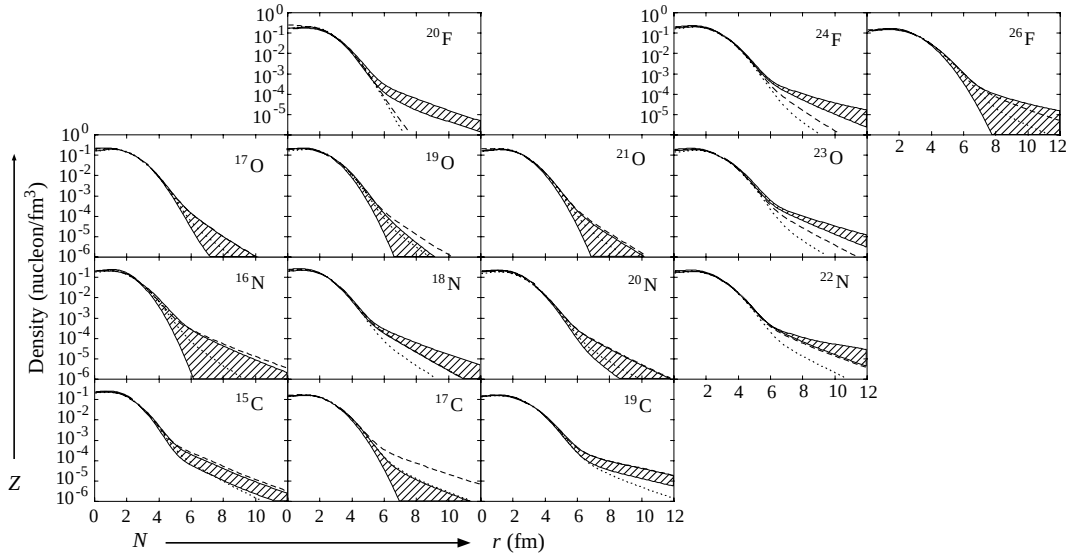


**Fig. 3.** Nucleon-density distributions for odd-$N$ nuclei in the light neutron-rich region. The dashed (dotted) line shows the density distributions deduced from a core plus $2s_{1/2}$ (a core plus $1d_{5/2}$) configuration using the experimentally observed neutron separation energies. The hatched area shows the density distribution required to reproduce the observed $\sigma_{\rm I}$ for both the core and the respective nucleus.

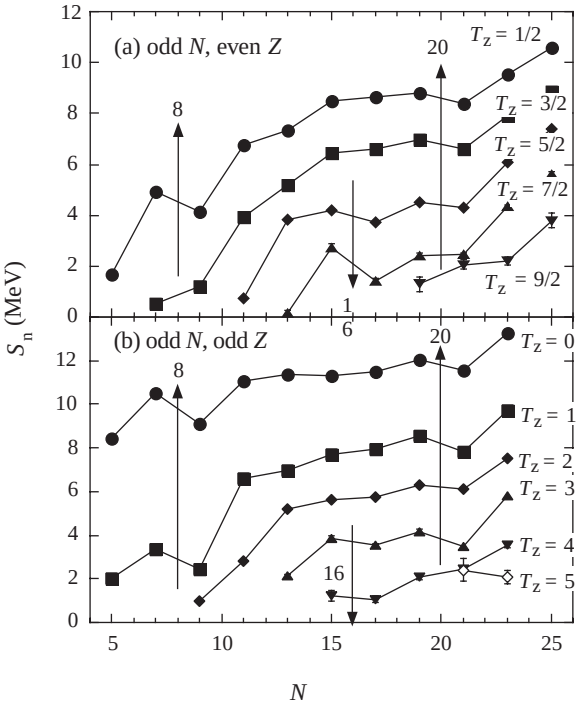


**Fig. 4.** Neutron ($N$) number dependence for experimentally observed neutron separation energies ($S_{\rm n}$) for nuclei with odd $N$ and even $Z$ (a) and odd $N$ and odd $Z$ (b), respectively.

given values of the separation energy. Equation (4) can be used to calculate $\sigma_{\rm I}$ using wave functions obtained by the code and the known core density ($^{A-1}Z$). In order to reproduce the observed $\sigma_{\rm I}$ of the respective nuclei ($^{A}Z$), we can change the wave functions (densities) for the valence nucleon. Finally, we deduce the densities for the respective nuclei by adding the resulting single-nucleon distribution to the core density distribution, taking into account the difference in the center of mass for the composite system.

A core-plus-neutron assumption allows one to deduce the effective densities for neutron-rich nuclei with an odd neutron number, using the GMFB. The effective density deduced by this analysis gives results consistent with those deduced by the energy dependence of $\sigma_{\rm I}$, for $^{11}$Be [8]. This analysis was applied to light neutron-rich nuclei. The results are shown in fig. 3 [8]. A neutron halo structure can be clearly seen for $^{19}$C, $^{22}$N, $^{23}$O and $^{24}$F.

In this analysis, we can deduce the spectroscopic factor ($S$-factor) for some halo nuclei. The deduced $S$-factor for $^{19}$C is consistent with the value given in ref. [9]. However, the authors in ref. [9] claimed $S_{\rm n}$ of $^{19}$C to be $530 \pm 130$ keV, whereas we adopted $S_{\rm n} = 0.24$ MeV for the present analysis. If we use $S_{\rm n} = 0.5$ MeV, the $S$-factor ($2s_{1/2}$) deduced by GMFB would be close to 1.0. However, even in this case, the tail of the deduced density of $^{19}$C is not changed. No configurations with a different relative strength of $s$ and $d$ waves are able to simultaneously reproduce the $\sigma_{\rm I}$ and the longitudinal momentum distribution. A detailed discussion of the possible nuclear structure for $^{19}$C is given in refs. [10,11]. Further experimental studies, such as a determination of $J^{\pi}$ and more reliable mass measurements, are needed before any conclusive statement concerning the halo structure of $^{19}$C can be made.

### 3.3 New magic number, N = 16, near the neutron drip line

Recently, the neutron separation energies ($S_{\rm n}$) and the $\sigma_{\rm I}$ for neutron-rich $p$-$sd$ and $sd$ shell region have been surveyed in order to search for a new magic number [12].

A neutron ($N$) number dependence of experimentally observed $S_{\rm n}$ for nuclei with odd $N$ and even $Z$ (odd $N$ and odd $Z$) is shown in fig. 4 [13]. The $N$-number dependence of $S_{\rm n}$ shows clear breaks at $N = 16$ near to the neutron drip line, which shows the creation of a new magic number. The $N$-number dependence of $\sigma_{\rm I}$ shows a large increase of $\sigma_{\rm I}$ for neutron-rich $N = 15$, which supports the new magic number, as follows. As can be seen in fig. 5, the observed $\sigma_{\rm I}$ can be reproduced only using the $2s_{1/2}$ orbital. For the case of the $1d_{5/2}$ orbital, we cannot reproduce the observed $\sigma_{\rm I}$, even if we use $S_{\rm n} = 0$ MeV, as shown by the dashed lines in fig. 5. Thus, we conclude a dominance of the $2s_{1/2}$ orbital for the valence neutron in $^{22}$N, $^{23}$O and $^{25}$F. On the other hand, the increase of $\sigma_{\rm I}$ from $^{25}$Na to $^{26}$Na can be explained by mixing the $2s_{1/2}$ and $1d_{5/2}$ orbitals, as shown in fig. 5. We could not perform a meaningful analysis for Ne and Mg isotopes because of the relatively large error bars for $\sigma_{\rm I}$. However, the rates for the increase of $\sigma_{\rm I}$ for the isotopes are also similar to those for the Na-isotopes. Thus, we also conclude that a valence neutron for $^{25}$Ne and $^{27}$Mg is a mixing of the $2s_{1/2}$ and $1d_{5/2}$ orbitals. Thus, the purity of $2s_{1/2}$ drastically increases near to the drip line for $N = 15$ nuclei. This conclusion supports the creation of a new magic number at $N = 16$ near to the neutron drip line, since a clear single-particle structure is suggested for $N = 15$ nuclei near to the drip line. The origin of this new magic number may be due to neutron halo formation. At weakly bound $N = 16$, the $2s_{1/2}$ and $1d_{5/2}$ orbitals are filled by neutrons leaving a large gap in the $1d_{3/2}$ orbital.

### 3.4 Proton skin for Ar isotopes

From the measured $\sigma_{\rm I}$ for Ar isotopes ($A$ = 31 to 40), we can deduce the effective RMS matter radii. The RMS charge radii for Ar isotopes ($A$ = 32 to 40) are already known [14]. Thus, by combining RMS matter and RMS charge radii, we can deduce the effective RMS neutron radii for Ar isotopes ($A$ = 32 to 40). Since preliminary data of $\sigma_{\rm I}$ have relatively large errors, we cannot see any clear neutron dependence of RMS neutron radii. Further analysis will show a clear dependence and possibly the proton skin thickness for proton-rich Ar isotopes.

## 4 Summary

Measurements of the interaction cross-sections ($\sigma_{\rm I}$) have been made by a transmission method at relativistic energies. At the FRS in GSI, recent experiments have been performed for mainly light nuclei up to F.

Recently, the Glauber model for a few-body system has been developed. An analysis allows one to deduce the effective nucleon density distributions and spectroscopic factor for halo nuclei. It is noted that a halo structure of $^{19}$C is clearly shown by an analysis, although further experimental and theoretical studies are necessary to determine the structure in detail.

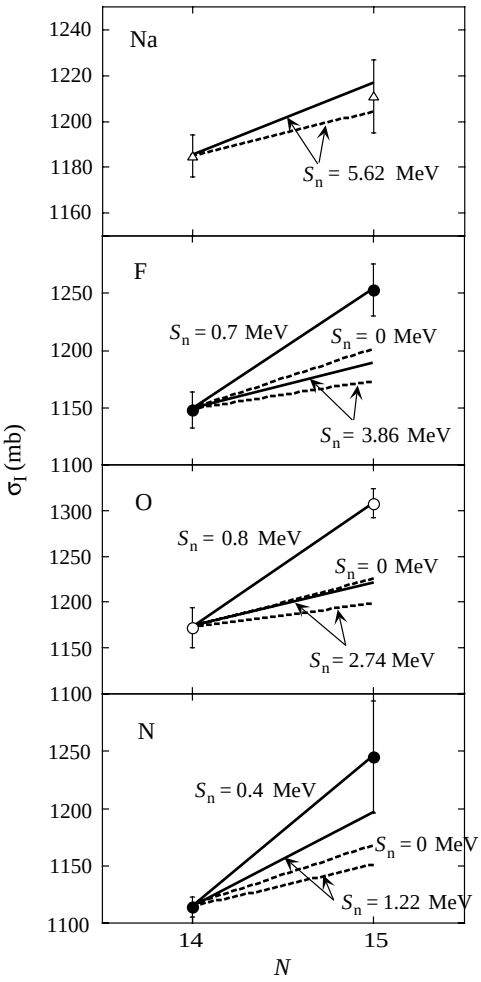


**Fig. 5.** $\sigma_{\rm I}$ for nuclei with $N$ = 14,15 on C targets. The solid (dashed) lines show the increase of $\sigma_{\rm I}$ calculated by Glauber model calculations for few-body systems assuming a pure $2s_{1/2}$ ($1d_{5/2}$) orbital for the valence neutron with given neutron separation energies ($S_{\rm n}$), respectively. The unit of $S_{\rm n}$ is given by MeV.

Recently, a new magic number, $N = 16$, near the neutron drip line is shown by the neutron number dependence of the neutron separation energies. The $\sigma_{\rm I}$ values for $N = 15$ isotopes ($^{22}$N to $^{24}$F) are larger than those of $N = 14$ nuclei, which also supports the magic number.

Very recently, the $\sigma_{\rm I}$ values for Ar isotopes have been measured. By combining their known charge radii, we can deduce the neutron radii. Thus, we can deduce the proton skins for Ar isotopes. Further analysis will reveal the thickness of the proton skins.

## References

1. I. Tanihata *et al.*., Phys. Rev. Lett. **55**, 2676 (1985).
2. G. Huber *et al.*., Phys. Rev. C **18**, 2342 (1978).
3. T. Suzuki *et al.*., Phys. Rev. Lett. **75**, 3241 (1995).
4. H. Geissel *et al.*, Nucl. Instrum. Methods B **70**, 286 (1992).
5. J.S. Al-Khalili, J.A. Tostevin, Phys. Rev. Lett. **76**, 3903 (1996).
6. Y. Ogawa *et al.*, Nucl. Phys. A **543**, 722 (1992).

7. M.M. Obuti *et al.*, Nucl. Phys. A **609**, 74 (1996).
8. A. Ozawa *et al.*, Nucl. Phys. A. **691**, 599 (2001).
9. T. Nakamura *et al.*, Phys. Rev. Lett. **83**, 1112 (1999).
10. T. Baumann *et al.*, Phys. Lett. B **439**, 256 (1998).
11. R. Kanungo *et al.*, Nucl. Phys. A **677**, 171 (2000).
12. A. Ozawa *et al.*, Phys. Rev. Lett. **84**, 5493 (2000).
13. G. Audi, A.H. Wapstra, Nucl. Phys. A **595**, 409 (1995).
14. A. Klein *et al.*, Nucl. Phys. A **607**, 1 (1996).